

In situ strategy for biomedical target localization via nanogold nucleation and secondary growth

Akira Sawaguchi¹  [✉], Takeshi Kamimura², Nobuyasu Takahashi¹, Atsushi Yamashita³, Yujiro Asada³, Hiroyuki Imazato⁴, Fumiyo Aoyama¹, Akiko Wakui², Takeshi Sato², Narantsog Choijookhuu⁵ & Yoshitaka Hishikawa⁵

Immunocytochemistry visualizes the exact spatial location of target molecules. The most common strategy for ultrastructural immunocytochemistry is the conjugation of nanogold particles to antibodies as probes. However, conventional nanogold labelling requires time-consuming nanogold probe preparation and ultrathin sectioning of cell/tissue samples. Here, we introduce an in situ strategy involving nanogold nucleation in immunoenzymatic products on universal paraffin/cryostat sections and provide unique insight into nanogold development under hot-humid air conditions. Nanogold particles were specifically localized on kidney podocytes to target synaptopodin. Transmission electron microscopy revealed secondary growth and self-assembly that could be experimentally controlled by bovine serum albumin stabilization and phosphate-buffered saline acceleration. Valuable retrospective nanogold labelling for gastric H⁺/K⁺-ATPase was achieved on vintage immunoenzymatic deposits after a long lapse of 15 years (i.e., 15-year-old deposits). The present in situ nanogold labelling is anticipated to fill the gap between light and electron microscopy to correlate cell/tissue structure and function.

¹Division of Ultrastructural Cell Biology, Department of Anatomy, University of Miyazaki, Miyazaki, Japan. ²Hitachi High-Tech Corporation, Tokyo, Japan. ³Division of Pathophysiology, Department of Pathology, University of Miyazaki, Miyazaki, Japan. ⁴Division of Orthopedic Surgery, Department of Medicine of Sensory and Motor Organs, University of Miyazaki, Miyazaki, Japan. ⁵Division of Histochemical Cell Biology, Department of Anatomy, University of Miyazaki, Miyazaki, Japan. [✉]email: akira_sawaguchi@med.miyazaki-u.ac.jp

One of the major goals of morphological biology is to identify correlations between cell/tissue structures and functions. Visualization of the exact location of targeting molecules presents unique spatial information that no other biomedical analysis can provide. This process is called immunocytochemistry, a combination of immunochemistry and cell morphology, which uses specific antibodies against the target molecules of interest. In the last decade, many cell biologists have used immunocytochemistry, which has the benefits of improved fluorescence light microscopy, such as two-photon excitation microscopy; however, owing to the limited spatial resolution of light microscopy, electron microscopy is often needed to address important questions¹. To close the gap between light and electron microscopy, researchers have recently used correlative light and electron microscopy (CLEM) to determine the orientation of complex cell/tissue architectures by light microscopy and identify ultrastructural correlations through electron microscopy².

Nanogold particles with diameters of 1–100 nm are also known as colloidal gold when dispersed in water. In 1857, Faraday first provided a scientific description of the optical properties of nanometer-scale gold synthesized by reducing chloroauric acid solution³. Since then, various experimental methods have been developed for the synthesis of nanogold particles based on Turkevich's pioneering study⁴ in 1951, which identified the nucleation and growth process in the synthesis of colloidal gold. Recently, nanogold particles have attracted increasing interest because of their potential in nanotechnology-based on their unique size and three-dimensional structure^{5,6}.

In 1959, Singer⁷ first reported an antibody tagged with the electron-dense protein ferritin for immunocytochemistry because the electron-scattering ability of fluorescent probes is insufficient for electron microscopy. Since the report by Faulk and Taylor in 1971⁸, the general strategy for electron microscopic localization is the conjugation of nanogold “probes” to antibodies^{9,10}. The nanogold probes are easily distinguished on the labeled cell/tissue structures and can be counted for quantitative analysis of labeling intensity. However, conventional methods require the time-consuming preparation of nanogold probes^{11,12} and their conjugation to antibodies^{9,10}. A variety of nanogold-conjugated antibodies are commercially available to decrease preparation, but ultrathin sectioning of the cell/tissue samples still requires time and skill for post-embedding nanogold probe labeling.

In a previous study¹³, we introduced an informative three-dimensional survey of complex cell/tissue architectures using low-vacuum scanning electron microscopy (SEM) accompanied by CLEM imaging. This study aimed to develop its application in immunocytochemical localization, which remains challenging owing to difficulties in achieving labeling intensity with large particles. There is a trade-off relation between large particles and labeling intensity in post-embedding nanogold probe labeling¹⁴, but large particles (>30 nm) are indispensable for visualization under low-vacuum SEM. In this context, we introduce a new strategy involving *in situ* nanogold nucleation in immunoenzymatic 3,3'-diaminobenzidine tetrahydrochloride (DAB) products on universal paraffin/cryostat sections and provide novel insight into nanogold development in hot-humid air conditions for ultrastructural localization.

Results and discussion

Practical *in situ* nanogold labeling. The proposed procedure employs the catalytic properties of an enzyme (horseradish peroxidase; HRP) that yields a red/brown-colored reaction product from DAB¹⁵. Compared with immunofluorescence, the enzyme system¹⁶ is advantageous in that the resultant precipitates remain permanent and visible under a standard

bright-field light microscope. Fig 1 illustrates the flow diagram from the light microscopic survey to the correlative ultrastructural localization of the target molecules (in this experiment, synaptopodin¹⁷, expressed in the process of podocytes in the kidney glomerulus). After the light microscopic survey and preselection, the sections were treated with 0.01% tetrachloroauric acid (HAuCl₄) for 10 min, leading to nanogold particle “nucleation” (Fig. 1a). Then, the sections were exposed to hot-humid air in a humid chamber at 37 °C for 9–15 h to accomplish the “secondary growth” of the nucleated nanogold particles around the target molecules.

For electron microscopic observation, one section was placed on the wide specimen stage of the low-vacuum SEM (Fig. 1b), which was suitable for the whole-section survey at the centimeter scale (larger than the limited millimeter scale for conventional electron microscopy). Low-vacuum SEM allows backscattered electron imaging of non-conductive biological samples because the negative charge accumulations on the non-conductive materials can be neutralized by the positive ions in residual gas molecules¹⁸. As shown in the representative electron micrographs, nanogold particles were specifically localized on the process of podocytes in the kidney glomerulus, consistent with the preselected light microscopic findings. The underlying fine structures of the podocytes and their processes, which were not observable with conventional light microscopy, were clearly observed at higher magnification.

Fortuitous nanogold development in a summer. The present *in situ* nanogold labeling was fortuitously developed on a laboratory bench, independent of previous studies. At the beginning of this study, we initially attempted to “enhance” the contrast of DAB deposition sites with 0.1% HAuCl₄ solution to convert the color signal into an electron-dense compound for electron microscopy^{19,20}. It has been reported that exposure to gold chloride intensifies the electron density of DAB deposition sites¹⁹. In our early trials, however, the enhanced signals were indistinguishable from the enhanced electron emission, known as the edge effect, generated along the sectioned cell/tissue edges (Fig. 2a). The disappointing section was left on our laboratory bench over a hot-humid summer weekend. As a result, the section color unexpectedly changed from yellow to purple, indicating the development of nanogold particles³. Further experiments demonstrated a constant color change (Fig. 2b) and indicated nanogold labeling (Fig. 2c) accompanied by undesirable non-specific particles owing to an unrefined preliminary protocol.

Historically, the protocol for newly synthesized nanogold particles has been developed by extensive trial-and-error strategies rather than directed design^{4–6}. In this study, the nanogold labeling efficiency and specificity were optimized by coordinating the HAuCl₄ concentration, treatment time, and subsequent hot-humid incubation. First, the optimal combination was determined in the range of 0.02–0.01% HAuCl₄ and 3–20 min by first performing hot-humid development at 37 °C for 12 h (Fig. 2d–g). Next, the optimal hot-humid development time was identified in the range of 9–15 h for standardized treatment with 0.01% HAuCl₄ for 10 min (Fig. 3). Finally, the optimal temperature was determined to be 37 °C for hot-humid development by the elimination of unsatisfactory development at 18 °C and morphological destruction at 60 °C (Fig. 3). Indispensably, the cell/tissue structures must be visible under ideal nanogold labeling to enable exact localization.

***In situ* nanogold nucleation on the target site.** Transmission electron microscopy (TEM) was applied to precisely localize the nanogold particles and define their morphological features at

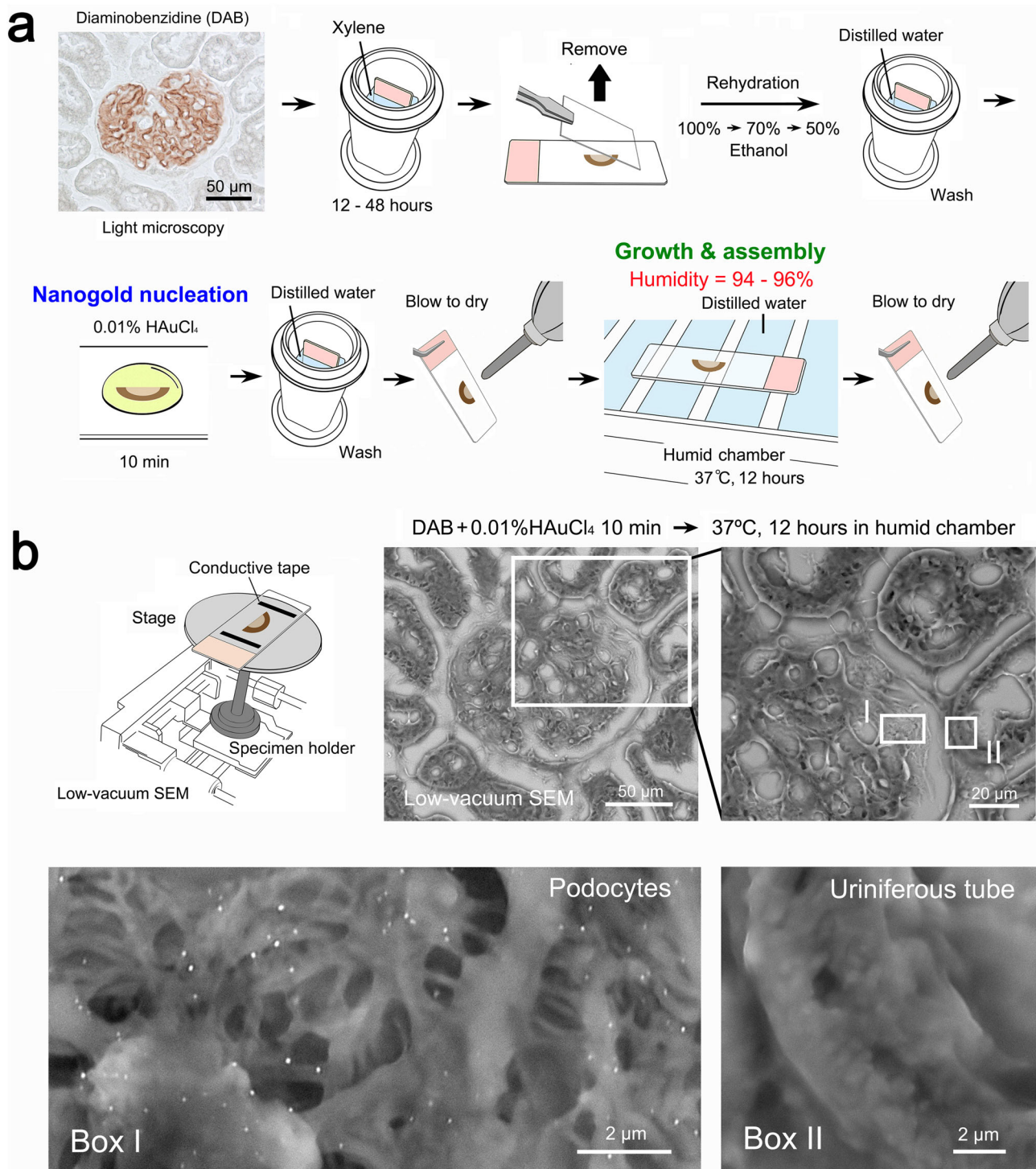


Fig. 1 Practical flow diagram of in situ nanogold labeling and representative electron micrographs. a First, the DAB deposition sites for the target molecules were surveyed under a light microscope. Then, the preselected microscope slides were incubated in xylene for 12–48 h to remove the coverslips and then rehydrated through an ethanol series. After the sections were washed in distilled water, they were treated with 0.01% HAuCl₄ for 10 min and then incubated in a humid chamber (with distilled water [DW] on the floor) at 37 °C for 12 h. **b** One microscope slide was placed on the wide stage of the specimen holder for low-vacuum SEM. The electron micrographs showed specific labeling on the processes of podocytes in the kidney glomerulus (in Box I), demonstrated by correlative light and electron microscopy (compare to the light micrograph in **a**). The cuboidal epithelium of the uriniferous tube, as a negative control, shows no particles (in Box II).

high resolution. The nanogold particles developed in situ were specifically localized in the processes of podocytes (Fig. 4a), consistent with the original report by conventional immunogold labeling¹⁷. The underlying processes of nanogold particle formation could be explained by LaMer’s classic theory²¹ and its

modifications, which have described the concept of burst nucleation as the first step in a phase transition. Consequently, the nucleated particles act as “seeds” for the secondary growth induced by a combination of monomer addition, aggregation, and coalescence.

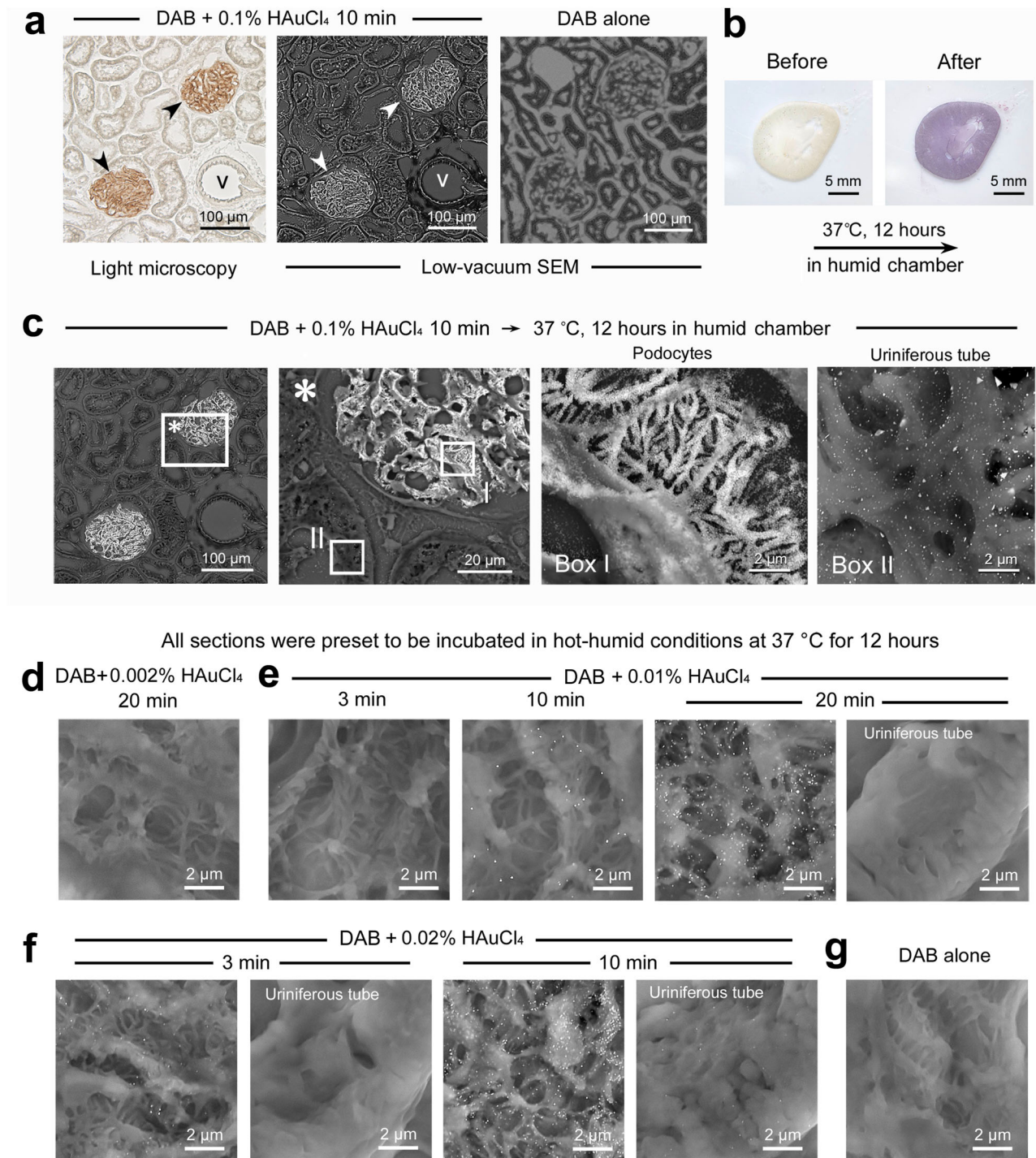


Fig. 2 Prototype of the in situ nanogold labeling and coordination of HAUCl₄ concentration and treatment time. **a** Contrast enhancement with 0.1% HAUCl₄ for the DAB deposition sites (arrowheads). Note the undifferentiated enhancement at the contours of the uriniferous tube and the blood vessel (v) caused by the edge effect under low-vacuum SEM. **b** Optical color change in the cell/tissue section after hot-humid incubation at 37 °C for 12 h. **c** Low-vacuum SEM images of the color-changed section. Note the intense nanogold labeling on the DAB deposition sites (in Box I) and nonspecific particles over the uriniferous tube (in Box II). **d-g** All sections were preset to be incubated in hot-humid conditions at 37 °C for 12 h. **d, e** Nanogold labeling was insufficient after treatment with 0.002% HAUCl₄ for 20 min (**d**) and 0.01% HAUCl₄ for 3 min compared with the standard treatment with 0.01% HAUCl₄ for 10 min (**e**). Intense labeling was obtained with 0.01% HAUCl₄ for 20 min, but it obscured the underlying fine structure of the podocyte process. **f** Appropriate labeling was obtained with 0.02% HAUCl₄ for 3 min, but the short elongation of 10 min caused nonspecific particles on the uriniferous tube. **g** DAB alone as a negative control.

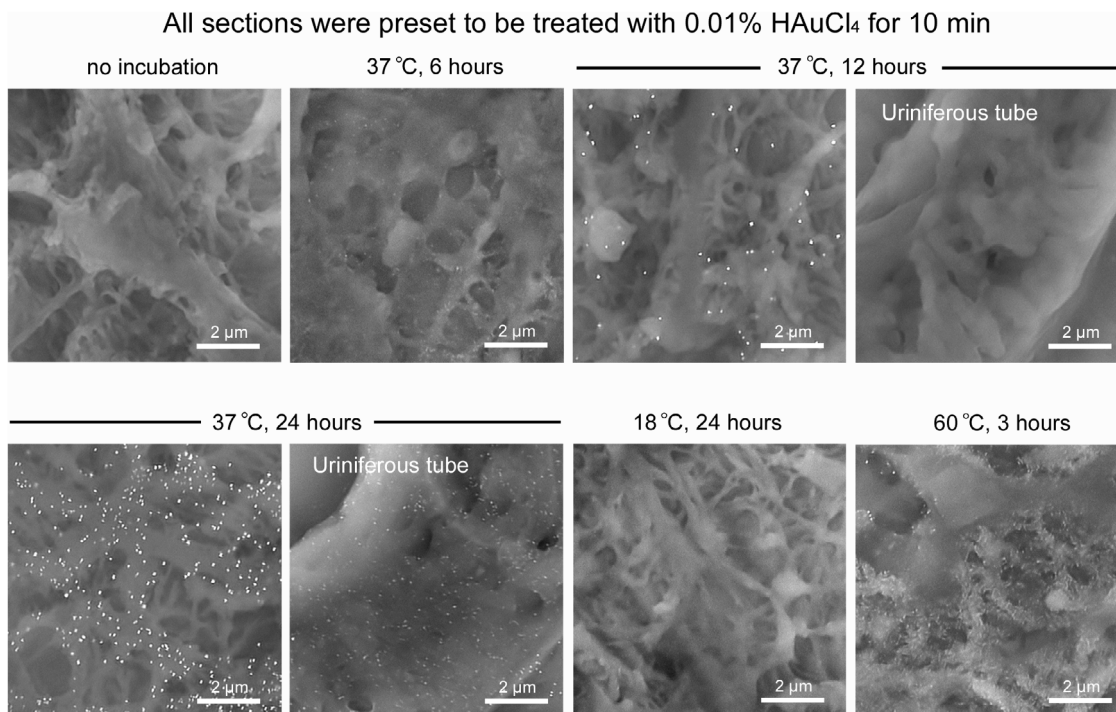


Fig. 3 Coordination of the duration and temperature of hot-humid incubation. All sections were preset to be treated with 0.01% HAuCl₄ for 10 min. Note the immature growth of nanogold particles after hot-humid incubation at 37 °C for 6 h. Satisfactory labeling was observed after 12 h, but elongation to 24 h caused nonspecific particles on the urineriferous tube. No labeling was developed in the humid chamber at 18 °C for 24 h. Incubation at 60 °C accelerated nanogold development, but the underlying structure of the podocyte process was significantly damaged.

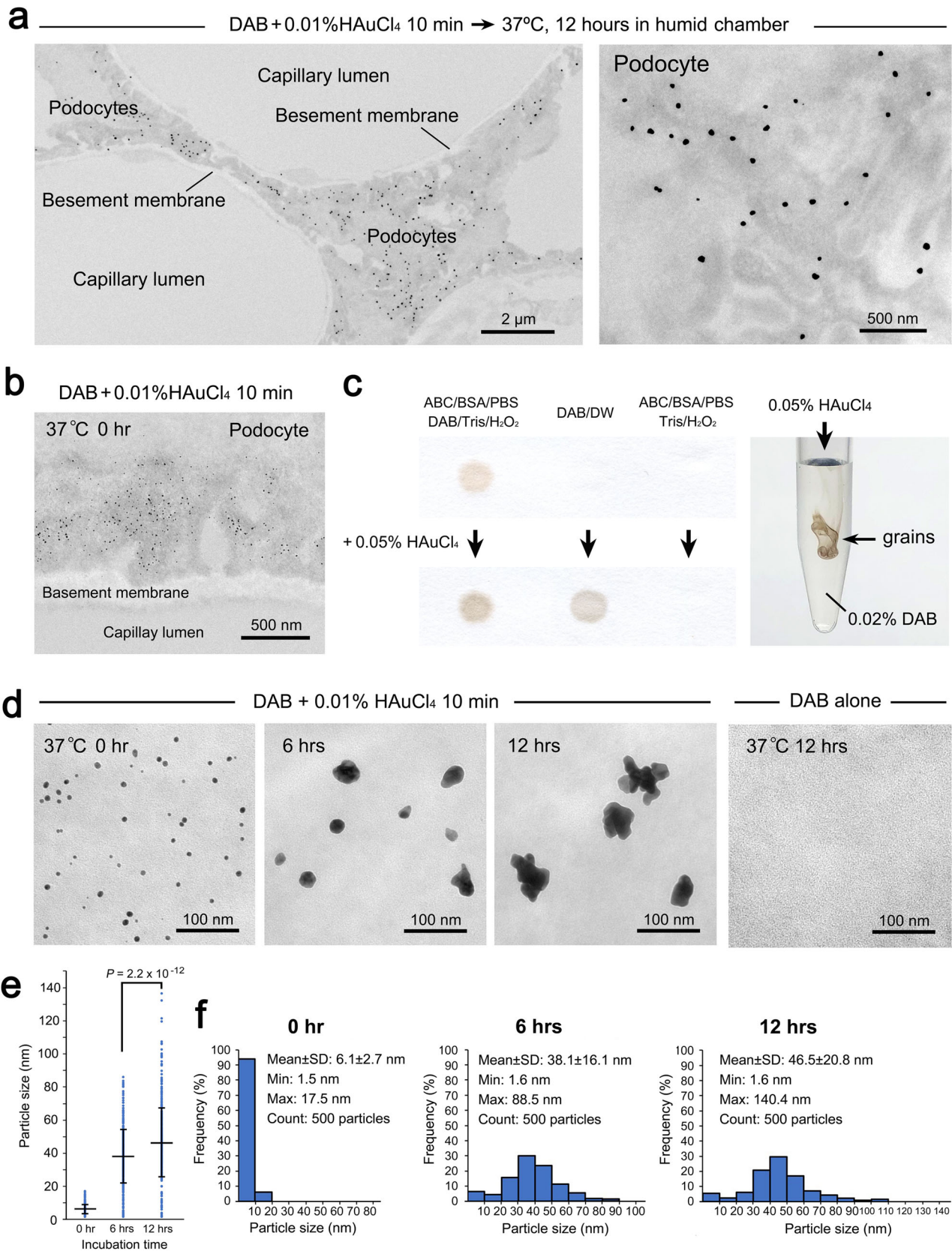
In this study, the primary step of nanogold particle “nucleation” was confirmed among the immunoenzymatic DAB products for the target molecules after treatment with 0.01% HAuCl₄ alone for 10 min (Fig. 4b). The speculated reactivity between HAuCl₄ and DAB was verified by dot blotting on filter paper²⁰ (Fig. 4c) and by dripping 0.05% HAuCl₄ into 0.02% DAB aqueous solution, which produced brown grains in a microtube. In immunohistochemical staining, DAB is known to be oxidized by hydrogen peroxide (H₂O₂) in the presence of HRP that forms a brown deposition, representing the location of the HRP for light microscopy. Intensifications of DAB deposition sites have been reported with various heavy metallic ions as well as gold chloride^{19,20,22–25}. The crucial binding ability between gold chloride and the immunochemical reaction product of DAB has been indicated by energy dispersive X (EDX)-ray analysis²⁵. Interestingly, oxidative polymerization of DAB on gold electrode has been reported in an electrochemical study for the preparation of polymeric film coated electrode²⁶. However, further analysis is needed due to the lack of detailed knowledge concerning DAB polymerization and the chemical characteristics of the resultant deposition in immunohistochemistry.

Secondary growth in hot-humid air conditions. An advanced series of TEM images demonstrated the secondary growth of nanogold particles via seed-mediated “monomer addition”, “aggregation”, and “coalescence” in accordance with LaMer’s theory^{4,5,21,27} (Fig. 4d). The secondary growth resulted in a significant increase in the average diameter (Fig. 4e) accompanied by a broadening of the size distribution (Fig. 4f). Concerning the gold source for monomer addition, elemental analysis indicated that the sections were equally stained with HAuCl₄ regardless of the DAB deposition sites (Fig. 5a). It could be assumed that gold monomers were supplied from the overall staining to the nanogold particles by liquid diffusion because the microscope slides

were moistened after the hot-humid incubation. In fact, the secondary growth failed in incubation in dry air, which might lack the dissolved gold monomers, and in waterdrop incubation, which might dilute the dissolved gold monomers (Fig. 5b).

Further TEM revealed the changes in nanogold configurations from spherical to multibranch polynuclear assemblies (alternatively referred to as gold nanostars²⁸ and nanoflowers²⁹) and the associated merged lines³⁰ (Fig. 6a). High-resolution scanning transmission electron microscopy (HR-STEM) demonstrated representative bright-field and annular dark-field images of intense nanogold labeling on the processes of podocytes (Fig. 6b). Higher magnification clearly shows the details of multiple crystalline structures in the attachment region (Fig. 6c) and lattice fringes with interplanar spacing of 0.24 nm corresponding to Au (111) planes accompanied by fast Fourier transform (FFT) patterns (Fig. 6d). Recently, studies of aggregating motion have been advanced by in situ liquid-cell TEM nanotechnologies that enable the “real-time” observation of aggregating nanogold particle motion in a cluster^{31–34} and manipulation of individual particles by electron beam³⁵. It will be of great interest to apply such forefront technologies to elucidate the precise mechanism of secondary growth in hot-humid air conditions, reaching large-sized intense labeling in a short time.

Influence of pH on nanogold particle size. Nanogold particles are unstable and tend to aggregate at short interparticle distances, which has attracted increased attention in the field of colloid science. Notably, secondary growth was reproduced on a dot blotting spot by hot-humid incubation at 37 °C for 12 h (Fig. 6e), providing a new filter paper assay for this study. In this protocol, the cell/tissue sections were treated with H₂O₂ as usual in enzyme-based immunocytochemistry. It could be speculated that residual H₂O₂ readily reduced HAuCl₄ and accelerated secondary growth^{36–39}. However, this speculation was contradicted by the



nucleation and secondary growth observed in H₂O₂-free blotting spots.

It is well known that the chemical properties of HAuCl₄ solution depend on its pH^{26,39–41}. The primary screening by filter paper model assay showed a decline in the purplish tone in

proportion to increasing pH value (Fig. 7a). Correspondingly, the low-vacuum SEM (Fig. 7b) demonstrated the reduction in labeling intensity on the sections. Further TEM observations (Fig. 7c) and quantitative analysis (Fig. 7d, e) clarified the reduction in secondary growth, which could be explained by the

Fig. 4 TEM analyses of nanogold nucleation and secondary growth. **a** Ultrathin TEM images of the in situ nanogold labeling of synaptopodin treated with 0.01% HAuCl_4 for 10 min followed by hot-humid incubation at 37 °C for 12 h. Note the specific labeling on the processes of podocytes. **b** Nucleated nanogold particles after treatment with 0.01% HAuCl_4 for 10 min. **c** Visualization of the chemical reaction between HAuCl_4 and DAB on dot blots and in vitro. ABC avidin-biotin complex, BSA bovine serum albumin, PBS phosphate-buffered saline, DAB diaminobenzidine, DW distilled water. **d** Time-lapse growth and changes from spherical to multibranched shapes. **e, f** Quantitative comparison of the average diameter (**e**) and the size distribution (**f**) of the nanogold particles. $n = 500$ particles/group. All data are expressed as the standard deviation (SD) \pm mean. Statistical significance was assessed by Student's *t* test.

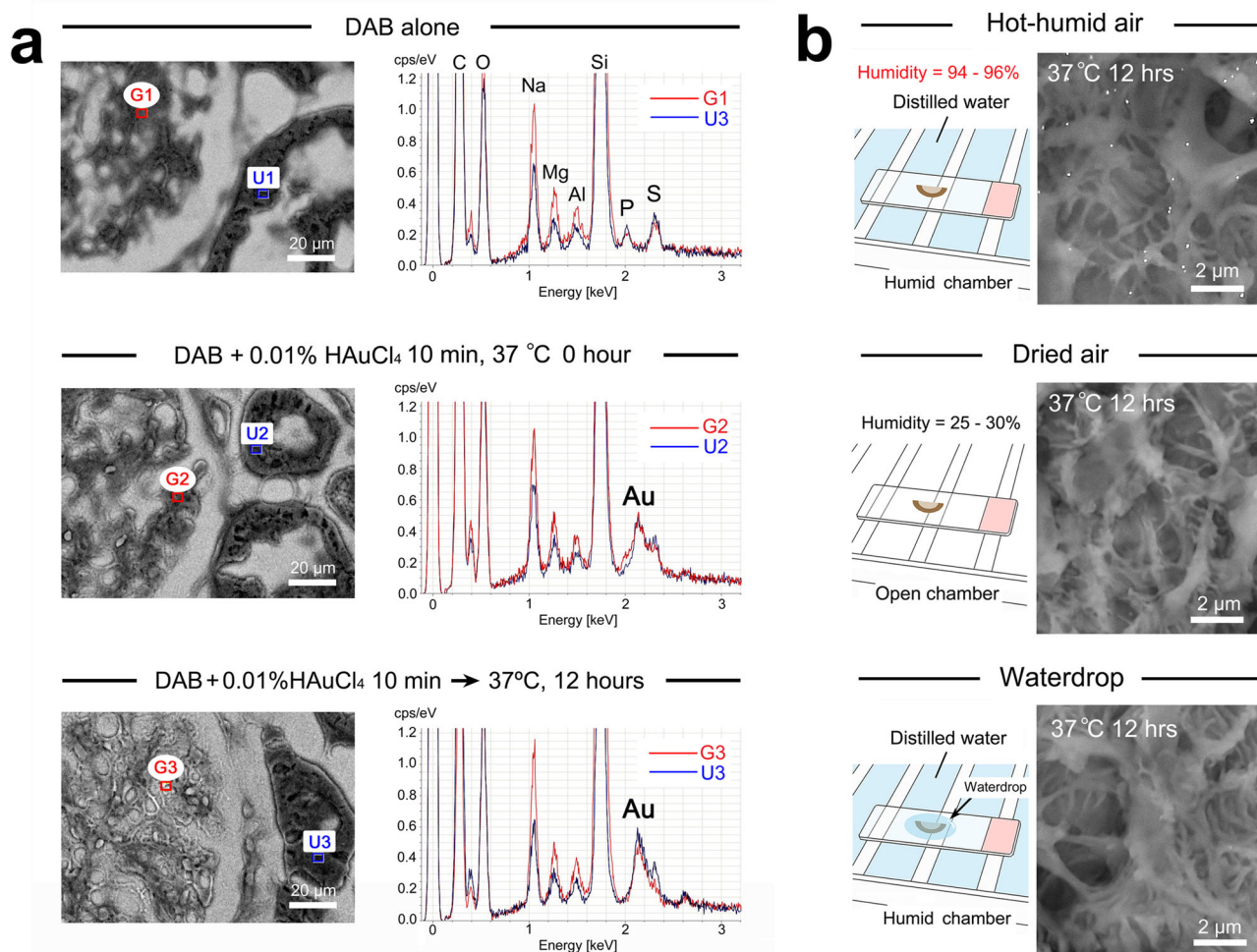


Fig. 5 Elemental analysis of Au distribution in the HAuCl_4 -treated sections and conditioning for secondary growth. **a** A clear Au peak emerged after treatment with 0.01% HAuCl_4 for 10 min compared with negative control of DAB alone. The Au peak levels were irrelevant to DAB deposition and equally observed in the glomerulus (G2) and uriniferous tube (U2). Note the unchanged Au peak pattern at G3 and U3 after hot-humid incubation at 37 °C for 12 h. G: glomerulus. U: uriniferous tube. **b** Conditioning for secondary growth. Distinct nanogold particles were developed in high-humidity air but not dried air or waterdrops and were incubated at 37 °C for 12 h.

stabilization of nanogold particles at higher pH, consistent with previous reports^{40–42}.

Experimental control of aggregation. Nanogold particles can be stabilized when macromolecules are adsorbed on the surface, creating a mechanical barrier against aggregation. Practically, bovine serum albumin (BSA) is added to solutions of antibody-conjugated nanogold particles as a “capping” agent in conventional methods^{10,12}. A filter paper assay showed a decline in the purplish tone after pretreatment with 2% BSA for 10 min prior to hot-humid incubation, indicating suppression of the secondary growth (Fig. 8a). Correspondingly, stabilization was proven on cell/tissue sections (Fig. 8b, c, e, f). HR-STEM revealed multiple

crystalline structures within the spherical particles (Fig. 8c), implicating polynuclear coalescence under suppression.

Successful stabilization has increased interest in destabilization by electrolytes that induce aggregation by reducing electrostatic repulsion⁴³. Indeed, pretreatment with phosphate-buffered saline (PBS) accelerated the growth and aggregation of nanogold particles, leading to massive polynuclear configurations (Fig. 8d, e, g). This series of experiments and findings will play an important role in verifying theoretical models for the process of nanogold particle development.

Potential in applied immunocytochemistry. Fig. 9a shows a diagram of the nanogold particle labeling originating from the in situ nucleation of immunoenzymatic DAB products, followed

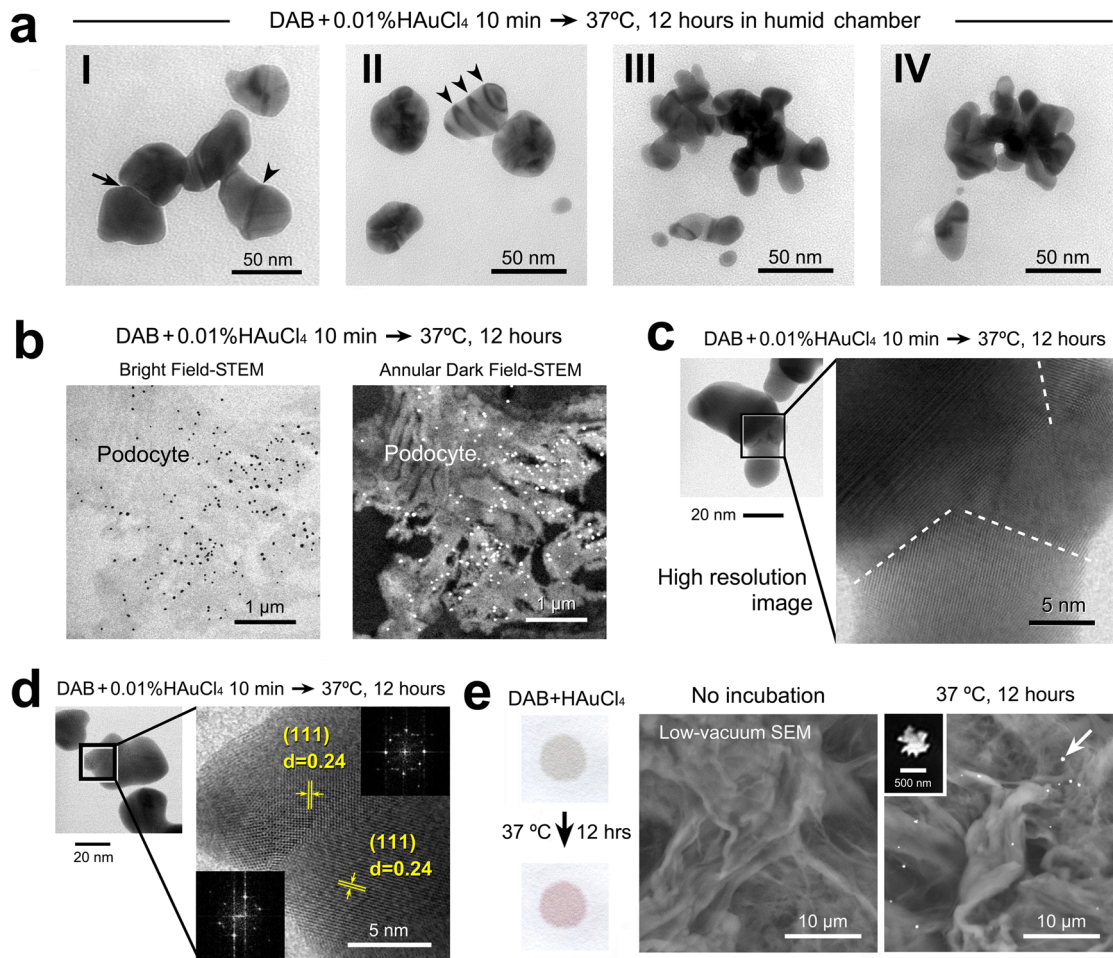


Fig. 6 The secondary growth and aggregation of nanogold particles. **a** Characteristic nanogold assemblies after hot-humid incubation at 37 °C for 12 h. **a-I** A representative branched feature of the nanogold particles. Note the attached portion (arrow) and merged line (arrowhead) within the assembly. **a-II** Heterogenous light and shade patterns are shown in each nanogold particle. Arrowheads indicate the stripe pattern at regular intervals. **a-III** Multibranch assembly. **a-IV** A multibranch assembly surrounding a hole. **b-d** HR-STEM images. Representative bright-field and annular dark-field images of intense nanogold labeling on the processes of podocytes (**b**). Higher magnification clearly shows the details of multiple crystalline structures in the attachment region (**c**) and lattice fringes (**d**) with interplanar spacing and FFT patterns. **e** A dot blotting spot exhibited a color change similar to that of cell/tissue sections after hot-humid air incubation at 37 °C for 12 h. The low-vacuum SEM micrographs show secondary growth on the filter paper with a representative “star-like” nanogold particle (inset).

by secondary growth and aggregation under hot-humid air conditions. This in situ nanogold labeling employed the catalytic properties of an enzyme that yields semipermanent precipitates on the target molecules. By taking advantage of this process, we achieved retrospective nanogold labeling of gastric H^+ / K^+ -ATPase on vintage DAB deposits after a long lapse of 15 years⁴⁴ (i.e., 15-year-old-DAB deposits, Fig. 9b; cf. Fig 3C in ref. 44). The paraffin and cryostat blocks of cell/tissue samples are semipermanent and show potential in retrospective investigations by the reappraisal of archived samples. The pathological application showed intense labeling of platelet glycoprotein IIb/IIIa preserved in an archived specimen of rabbit arterial thrombosis⁴⁵ (Fig. 9c). Moreover, this method can be combined with in situ hybridization, which enables the ultrastructural localization of a defined sequence of DNA or RNA on cell/tissue sections⁴⁶ (Fig. 10).

Recent advances in biomedical research, such as the production of regenerative organs from induced pluripotent stem cells and the morphological changes induced by CRISPR/Cas9-mediated genome editing, require the ultrastructural localization of a particular molecule to correlate cell/tissue structure and function. The present in situ nanogold labeling is user-friendly with basic

paraffin/cryostat sections and highly anticipated to create a new approach in applied biomedical immunocytochemistry, bridging the gap between light and electron microscopy.

Methods

Preparation of rat kidney cryostat sections. Male Wistar rats (Kyudo, Kumamoto, Japan) at 10 weeks of age were deeply anesthetized and then perfused with 4% paraformaldehyde in 0.1 M phosphate buffer (pH 7.4) from the left ventricle of the heart. The kidney was excised and further fixed by immersion in the above fixative for 2 h at room temperature (RT). After the organs were washed in running tap water for 2 h, they were protected in a graded series of 5%, 10 and 20% sucrose in PBS for 2 h and in a mixture of 1:1 (v/v) 20% sucrose:OCT compound (Sakura Finetek, Tokyo, Japan) at 4 °C overnight. The samples were then embedded in OCT compound and cut into sections (10 μ m in thickness) with a cryostat (CM3050 S, Leica Microsystems, Wetzlar, Germany).

Immunocytochemistry of synaptopodin. The cryostat sections of rat kidney were rinsed in PBS and then boiled in 10 mM citrate buffer, pH 6.0, for 10 min to retrieve the antigenic sites. After cooling to RT, the sections were incubated in methanol containing 0.3% H_2O_2 for 30 min to block endogenous peroxidase activity. After several rinses in PBS, the sections were incubated in 5% normal horse serum (NHS)/1% BSA in PBS for 10 min to block nonspecific binding and then incubated with a mouse monoclonal antibody against synaptopodin (clone G1D4; Progen Biotechnik, Heidelberg, Germany; diluted 1:50 with 5% NHS/1% BSA in PBS) at 4 °C overnight. As controls, the procedure was performed without

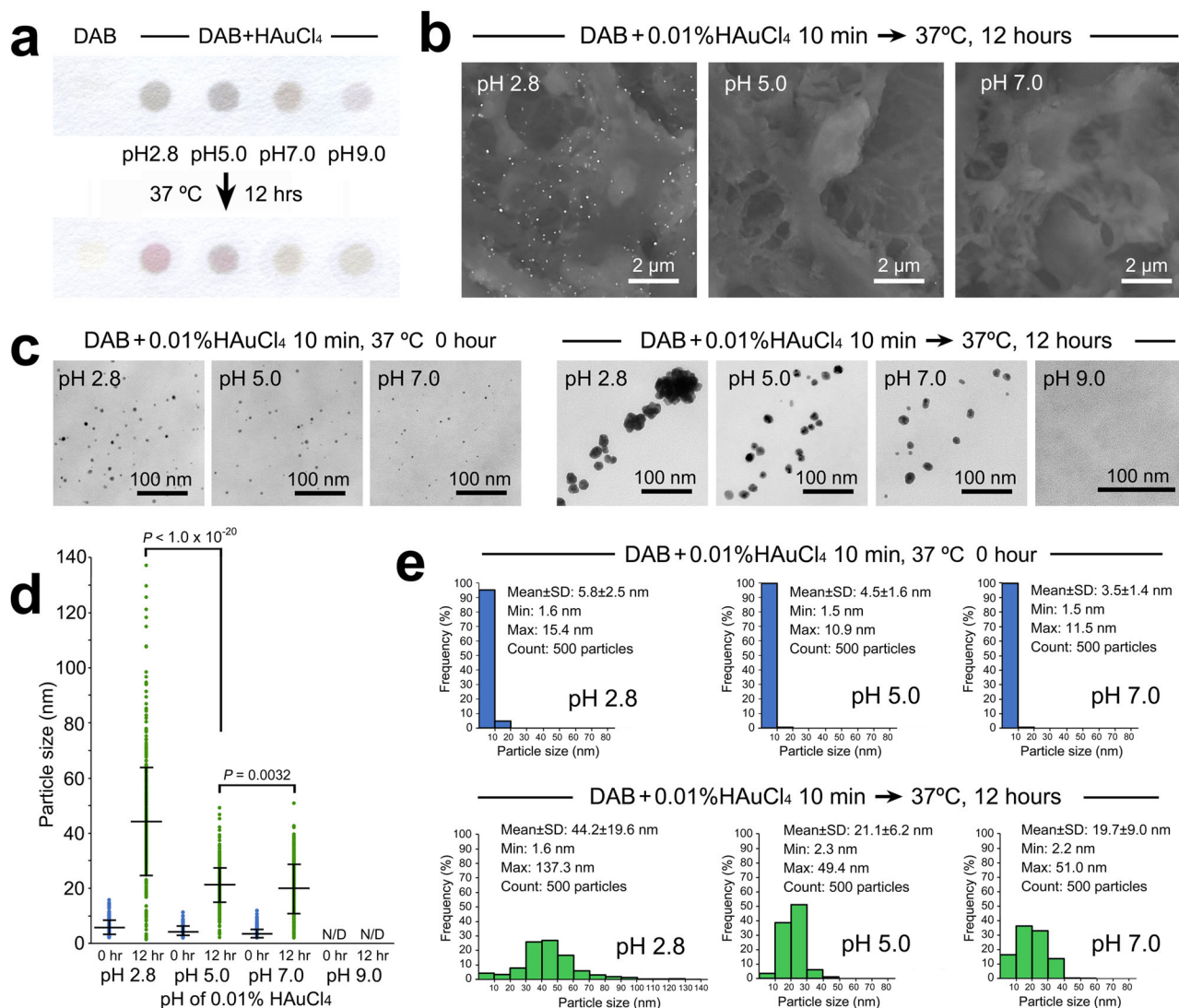


Fig. 7 Influence of pH on nanogold size. **a** Primary screening by filter paper model assay. Note the decline in the purplish tone in proportion to the increasing pH value of HAuCl₄ solutions. **b** Low-vacuum SEM. Note the satisfactory labeling at pH 2.8 and undistinguishable intensities at pH 5.0 and pH 7.0 after hot-humid incubation at 37 °C for 12 h. **c** Ultrathin TEM images of the nanogold particles before and after hot-humid incubation at 37 °C for 12 h. **d, e** Quantitative comparison of the average diameter (**d**) and size distribution (**e**) of the nanogold particles. $n = 500$ particles/group. All data are expressed as the standard deviation (SD) \pm mean. Statistical significance was assessed by Student's *t* test.

primary antibodies. After the sections were washed with PBS, they were incubated with biotinylated horse anti-mouse IgG (Vector Laboratories, Burlingame, CA, USA; diluted 1:200 with 1% BSA in PBS) at RT for 40 min, followed by washing with PBS. Then, sections were incubated in a freshly prepared solution of avidin-biotinylated HRP complex (ABC) kit (Vector Laboratories; diluted 1:50 with 1% BSA in PBS) for 30 min. After PBS washes, the peroxidase reaction was developed by incubating in 0.05% DAB (Dojindo Laboratories, Kumamoto, Japan) in 0.05 M Tris buffer, pH 7.6, containing 0.001% H₂O₂ for 8 min.

Light microscopic survey. For the light microscopic survey of the DAB deposition sites, the sections were rinsed in a graded series of 80%, 90%, and 100% ethanol for dehydration. After clearance in xylene, the sections were mounted within Malinol (Muto Pure Chemicals, Tokyo, Japan) covered with a NEO Micro cover glass (size 24 × 50 mm, thickness no. 1 = 0.13–0.17 mm; Matsunami Glass, Osaka, Japan). The DAB deposition sites were surveyed under a light microscope (BX51, Olympus, Tokyo, Japan) equipped with a digital camera (DP73, Olympus).

Nanogold particle development. Next, for light microscopy, the microscope slides were incubated in xylene for 18–48 h to remove the coverslips by dissolving the fixed mounting medium. Then, the sections were rehydrated with a series of 100%, 90%, and 70% ethanol (5 min each). After several rinses in distilled water (DW; at least three times, 5 min each), the sections were treated with a 0.01% aqueous

solution of hydrogen tetrachloroaurate (III) tetrahydrate (HAuCl₄·4H₂O, Nakarai Tesque, Kyoto, Japan) for 10 min at RT. After being rinsed several times in DW and dried, the sections were incubated in a humid chamber (equipped with DW on the floor, adequate humidity = 94–96%) at 37 °C for 12 h and then dried with a blower. As controls, other sections were incubated in dried air (humidity = 25–30%) or waterdrops.

The above optimal protocol was determined by the coordination of HAuCl₄ concentration (0.001, 0.002, 0.005, 0.01, 0.02, or 0.1%), HAuCl₄ treatment time (3, 5, 10, or 20 min), subsequent incubation time in a humid chamber (0, 3, 6, 9, 12, 15, 18, or 24 h) and temperature (18, 37, or 60 °C). The influence of the pH value on nanogold particle development was examined by changing the non-adjusted initial pH value of 0.01% HAuCl₄/DW (pH 2.8) to pH 5.0, pH 7.0, and pH 9.0 adjusted with 0.2 M K₂CO₃. The physicochemical properties of the nanogold particles were examined by treatment with 2% BSA/DW for 10 min or PBS for 10 min, followed by several rinses with DW prior to incubation in a humid chamber.

Low-vacuum SEM. The microscope slides were placed on the wide stage of the specimen holder using adhesive conductive tape and then placed in a low-vacuum SEM (TM4000Plus or TM3030Plus, Hitachi High-Tech, Tokyo, Japan) operating at 15 kV. Elemental analysis was performed by using an EDX detector equipped for low-vacuum SEM.

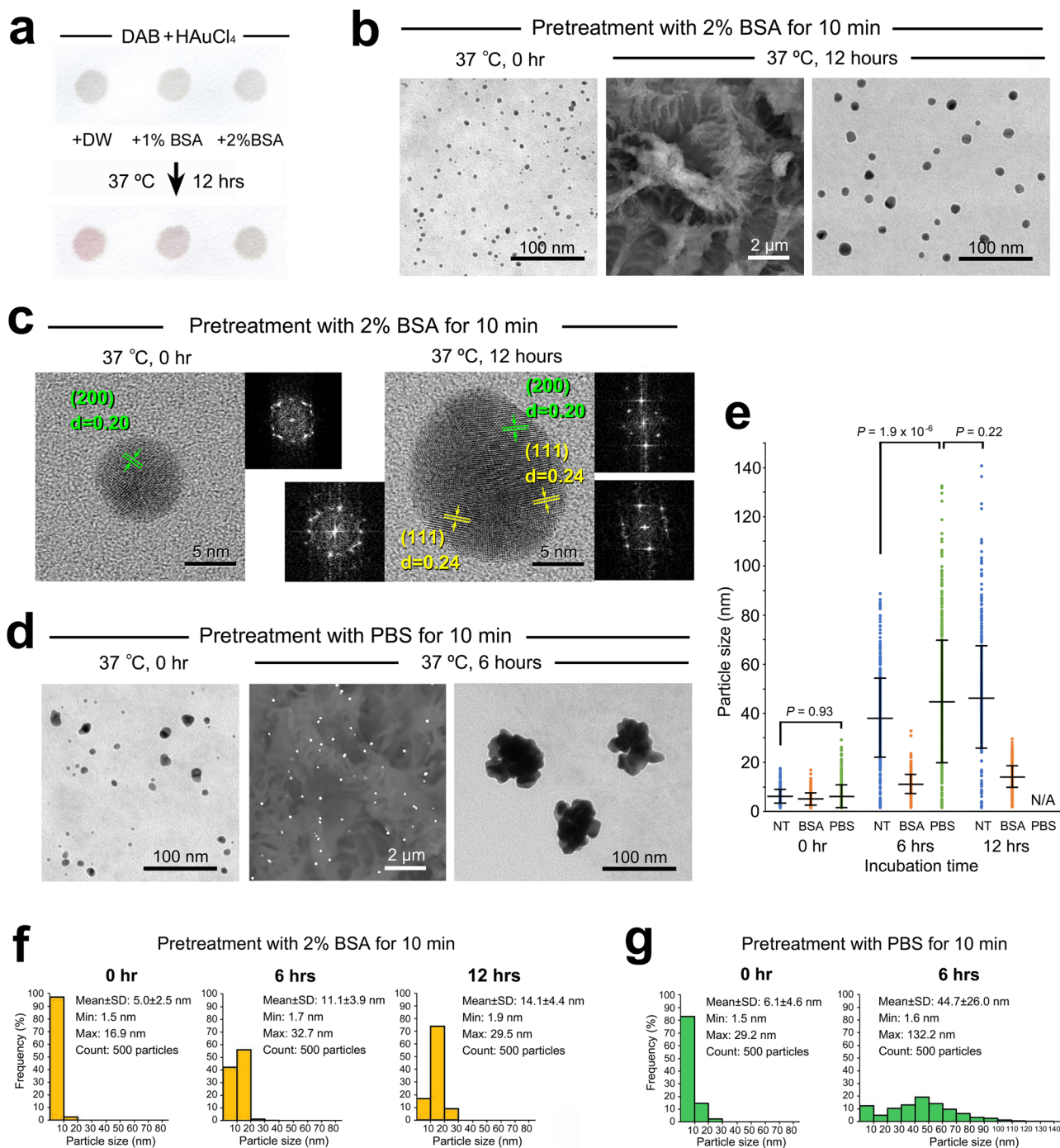


Fig. 8 Inhibition and acceleration of secondary growth after pretreatment with BSA and PBS. **a** Filter paper model assay for nanogold stabilization. Note the decline in the color change induced by pretreatment with 2% BSA for 10 min prior to hot-humid incubation. **b** Ultrathin TEM images of the nanogold particles after pretreatment with 2% BSA for 10 min prior to hot-humid incubation. Note that the secondary growth remained in a spherical form rather than a polynuclear configuration. **c** HR-STEM images of lattice fringes with interplanar spacing and FFT patterns. Note the multiple crystalline structures in the spherical particle after hot-humid incubation. **d** Pretreatment with PBS for 10 min accelerated growth and aggregation in polynuclear configurations. **e** Quantitative comparison of the average diameter. Because of the emergence of nonspecific particles, the average diameter was not applicable for 12 h of incubation after PBS pretreatment. NT not treated, N/A not applicable. **f** Size distribution of the nanogold particles after pretreatment with 2% BSA for 10 min prior to hot-humid incubation at 37 °C for 0, 6, and 12 h. **g** Size distribution after pretreatment with PBS for 10 min prior to hot-humid incubation at 37 °C for 0 and 6 h. Because of the emergence of nonspecific particles, the size distribution was not applicable for 12 h of incubation after PBS pretreatment. $n = 500$ particles/group. All data are expressed as the standard deviation (SD) \pm mean. Statistical significance was assessed by Student's *t* test.

Characterization of the developed nanogold particles. The nanogold particles were morphologically characterized by using a transmission electron microscope. For the characterization of nanogold particles, the sections were dehydrated in a graded series of 80%, 90%, and 100% ethanol and embedded into epoxy resin on microscope slides by using a capsule-supporting ring⁴⁷. Subsequently, the

polymerized resin block was removed from the microscope slide by rapid cooling in liquid nitrogen vapor. Ultrathin sections (60–80 nm in thickness) were cut and observed without heavy metal staining by using TEM (HT7700, Hitachi-High Tech, Tokyo, Japan) operating at 80 kV or HR-STEM (HD-2700A, Hitachi-High Tech, Tokyo, Japan) operating at 200 kV.

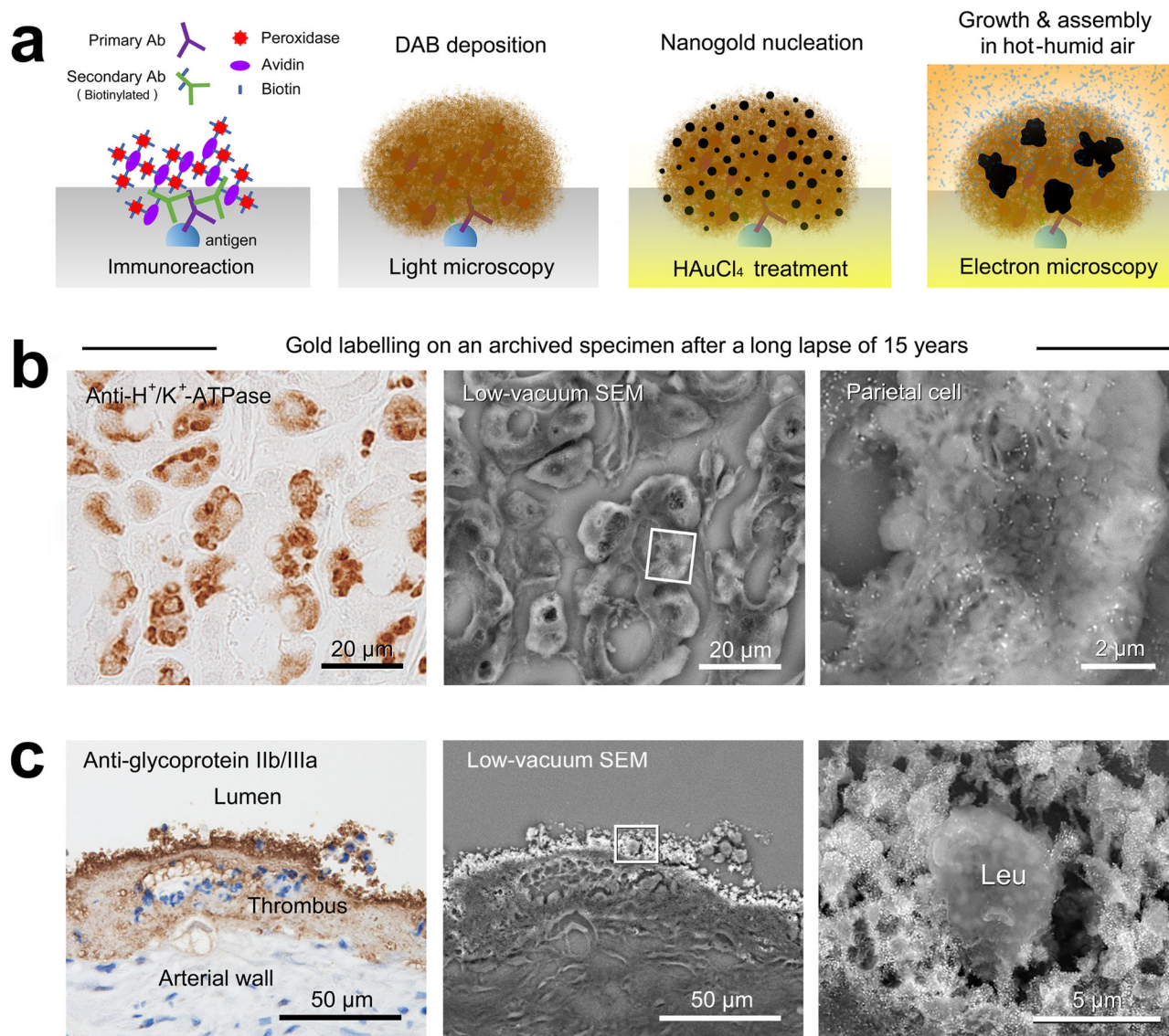


Fig. 9 Illustration of in situ nanogold labeling and biomedical applications. **a** Proposed illustration of the in situ nanogold labeling. Nanogold particles nucleated from HAuCl_4 in situ among the DAB deposition sites. The secondary growth and aggregation that occur in hot-humid conditions are sufficient for low-vacuum SEM observation. **b** Rat gastric parietal cell. Retrospective nanogold labeling of H^+/K^+ -ATPase on a valuable archived specimen after a long lapse of 15 years (i.e., 15 years old-DAB depositions). **c** Pathological application to rabbit arterial thrombosis. Note the intense labeling of glycoprotein IIb/IIIa expressed on the platelets surrounding the leukocyte (Leu). The cell nuclei were stained with hematoxylin for light microscopy.

Dot blot model analysis on filter paper. The reactivity of HAuCl_4 to DAB was verified by dot blotting¹⁹. First, one dot (2 μl aliquot) of 0.05% DAB in DW (Fig. 4c, middle) and two dots of the ABC kit reagent diluted 1:50 with 1% BSA/PBS were blotted on filter paper (No. 131, Advantec, Tokyo, Japan) as controls. Next, the latter two controls of the ABC kit/1% BSA/PBS dots were blotted with 0.05% DAB/0.05 M Tris buffer, pH 7.6/0.001% H_2O_2 (Fig. 4c, left), or 0.05 M Tris buffer, pH 7.6/0.001% H_2O_2 (Fig. 4c, right). Subsequently, all three dots were blotted with 0.05% HAuCl_4/DW and air-dried.

The resultant brown dots of 0.05% DAB/DW and 0.05% HAuCl_4/DW were clipped out and mounted on microscope slides using adhesive conductive tape. The development of nanogold particles was examined in a humidity chamber at 37 °C for 12 h, as described above for the cell/tissue sections. The influence of pH on nanogold particle development was examined by adjusting the initial pH value of 0.01% HAuCl_4/DW (pH 2.8) to pH 5.0, pH 7.0, and pH 9.0 with 0.2 M K_2CO_3 . The BSA stabilization test was performed with 1% or 2% BSA/DW by blotting over the brown dots of 0.05% DAB/DW and 0.05% HAuCl_4/DW prior to incubation in the humid chamber.

Application to archived immunocytochemical specimens. Archived paraffin sections of isolated gastric mucosa were employed from the immunocytochemical study by Sawaguchi et al.⁴⁴ (cf. Fig. 3C in ref. 44). In brief, a piece of isolated gastric mucosa was cryofixed in a liquid isopentane/propane mixture cooled by liquid

nitrogen. Freeze substitution was carried out in 0.1% glutaraldehyde in acetone at -80 °C for 16 h, and the specimen was then gradually warmed to RT. After the specimens were washed with ethanol, they were embedded in paraffin. Paraffin sections (5 μm in thickness) were deparaffinized, rehydrated, and incubated in methanol containing 0.3% H_2O_2 for 30 min. After several rinses in PBS, the sections were incubated in 5% NHS/1% BSA in PBS for 10 min to block nonspecific binding and then incubated with a mouse monoclonal antibody, 2B6, against H^+/K^+ -ATPase (MBL, Nagoya, Japan; 2 $\mu\text{g}/\text{ml}$ diluted with 5% NHS/1% BSA in PBS) at 4 °C overnight. After PBS washes, the sections were incubated with biotinylated horse anti-mouse IgG at RT for 40 min, followed by washing with PBS. Then, the sections were incubated in an ABC kit for 30 min. The samples were washed again with PBS, and the peroxidase reaction was developed as described above.

In addition to light microscopy, after a long lapse of 15 years from the original preparation, the microscope slides were incubated in xylene for 48 h to remove the coverslips. Then, the sections were rehydrated with a series of 100%, 90%, and 70% ethanol. After several rinses in DW, nanogold particles were developed as described above.

Application to pathological immunocytochemistry. Paraffin sections of rabbit arterial thrombosis were obtained from a disturbed blood flow model⁴⁵. In brief, the left femoral arteries of male Japanese white rabbits (Kyudo Corp, Kumamoto, Japan) weighing 2.5–3.0 kg were damaged by inserting a 2.5 (diameter) \times 9 (length)

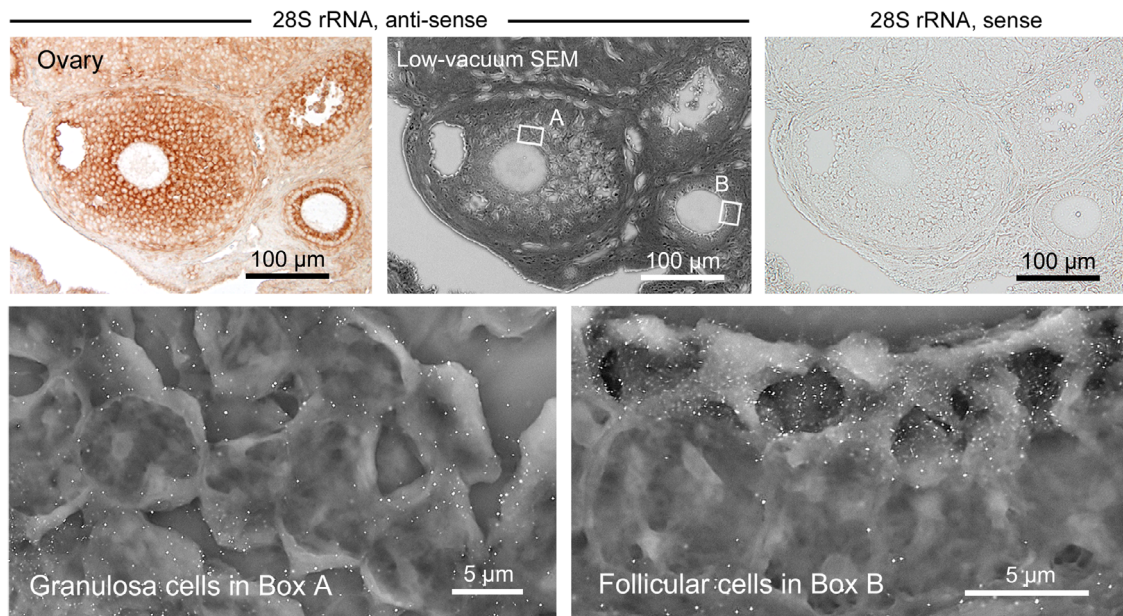


Fig. 10 Application of CLEM to in situ hybridization for gene targeting. CLEM was applied to in situ hybridization for gene targeting of 28 S rRNA on the mouse ovary. Note the intense nanogold labeling on the granulosa cells in Box A and the apical region of the follicular cells in Box B. The 28 S rRNA sense probe, as a negative control, showed no signal.

mm angioplasty balloon catheter (Boston Scientific, Galway, Ireland) into the femoral artery via the carotid artery. Three weeks later, the damaged femoral arteries were constricted to reduce the flow volume. Then, the rabbits were intravenously injected with heparin (500 U/kg) 15, 30, and 180 min thereafter, and then euthanized with an overdose of pentobarbital (60 mg/kg, intravenous) to evaluate thrombus formation. The animals were perfused with 4% paraformaldehyde, and the femoral artery was embedded in paraffin and sectioned (3 μm in thickness).

After deparaffinization, the sections were incubated in methanol containing 0.3% H₂O₂ for 30 min to block endogenous peroxidase activity. After several rinses in PBS, the sections were incubated in Protein Block (X0909; Agilent, Santa Clara, CA, USA) for 10 min to block nonspecific binding and then incubated with a sheep polyclonal antibody against the platelet glycoprotein IIb/IIIa (Affinity Biologicals, Inc., Hamilton, CA, USA; diluted 1:500 with Antibody Diluent purchased from Agilent) at 4 °C overnight. The procedure was performed without primary antibodies as a control. After the sections were washed with PBS, they were incubated with biotinylated donkey anti-sheep IgG (Jackson ImmunoResearch Laboratories, West Grove, PA, USA; diluted 1:1000 with Antibody Diluent) at RT for 30 min, followed by washing with PBS. Then, the sections were incubated in a ready-to-use solution of peroxidase-labeled streptavidin (Nichirei Biosciences, Tokyo, Japan) for 5 min. After the samples were washed with PBS, the peroxidase reaction was developed as described above. The cell nuclei were stained with Mayer's hematoxylin for 3 min and exposed to running tap water for at least 3 h to develop the color.

Application to in situ hybridization. Paraffin sections (5 μm in thickness) of the ovary from C57BL/6J female mice, 8–12 weeks of age, were prepared by chemical fixation with 4% paraformaldehyde in PBS at RT for 24 h. After deparaffinization, the sections were treated with 0.2 N HCl and digested with proteinase K. After postfixation with 4% paraformaldehyde in PBS for 5 min, the sections were immersed in 2 mg/ml glycine in PBS for 30 min and kept in hybridization medium, 40% deionized formamide in 4× standard saline citrate (SSC) (1× SSC = 0.15 M sodium chloride and 0.015 M sodium citrate, pH 7.0), until hybridization. Hybridization was carried out at 37 °C overnight with digoxigenin-labeled oligo-DNAs for 28 S rRNA (2173–2206) dissolved in hybridization medium⁴⁶. After repeated washings with 2× SSC, the sections were incubated with HRP-labeled sheep anti-digoxigenin antibody (Roche Diagnostics, Mannheim, Germany). After the samples were washed with PBS, the peroxidase reaction was developed as described above.

All animal procedures were carried out under protocols approved by the University of Miyazaki Animal Research Committee (#2005-009-1, #2016-513-3, #2016-509-5, #2018-509-1) in accordance with international guiding principles for biomedical research involving animals.

Statistics and reproducibility. In each experiment, the quantitative data were analyzed with 500 nanogold particles at random by using NIH ImageJ software (version 1.53c). The particle size was determined by the maximal Feret's statistical

diameter (i.e., the maximal perpendicular distance between parallel tangents touching opposite sides of the profile) (Supplementary Data 1). All data are expressed as the standard deviation ± mean. Statistical significance was assessed by Student's *t* test. *P* < 0.05 was considered statistically significant.

Reporting summary. Further information on research design is available in the Nature Research Reporting Summary linked to this article.

Data availability

Original light and electron micrographs and any other information are available upon request from the corresponding author.

Received: 23 November 2020; Accepted: 19 May 2021;

Published online: 10 June 2021

References

- Knott, G. & Genoud, C. Is EM dead? *J. Cell Sci.* **126**, 4545–4552 (2013).
- De Boer, P., Hoogenboom, J. P. & Giepmans, B. N. G. Correlated light and electron microscopy: ultrastructure lights up! *Nat. Methods* **12**, 503–513 (2015).
- Faraday, M. Experimental relations of gold (and other metals) to light. *Philos. Trans. R. Soc. Lond.* **147**, 145–181 (1857).
- Turkevich, J., Stevenson, P. C. & Hillier, J. A study of the nucleation and growth processes in the synthesis of colloidal gold. *Discuss. Faraday Soc.* **11**, 55–75 (1951).
- Polte, J. Fundamental growth principles of colloidal metal nanoparticles - a new perspective. *CrystEngComm* **17**, 6809–6830 (2015).
- Compton, O. C. & Osterloh, F. E. Evolution of size and shape in the colloidal crystallization of gold nanoparticles. *J. Am. Chem. Soc.* **129**, 7793–7798 (2007).
- Singer, S. J. Preparation of an electron-dense antibody conjugate. *Nature* **183**, 1523–1524 (1959).
- Faulk, W. P. & Taylor, G. M. An immunocolloid method for the electron microscope. *Immunocytochemistry* **8**, 1081–1083 (1971).
- Geoghegan, W. D. & Ackerman, G. A. Adsorption of horseradish peroxidase, ovomucoid and anti-immunoglobulin to colloidal gold for the indirect detection of concanavalin A, wheat germ agglutinin and goat anti-human immunoglobulin G on cell surfaces at the electron microscopic level: a new method, theory and application. *J. Histochem. Cytochem.* **11**, 1187–1200 (1977).
- De Mey, J. et al. High resolution light and electron microscopic localization of tubulin with the IGS (immuno gold staining) method. *Cell Biol. Int. Rep.* **5**, 889–899 (1981).

11. Frens, G. Controlled nucleation for the regulation of the particle size in monodisperse gold suspensions. *Nature* **241**, 20–22 (1973).
12. Slot, J. W. & Geuze, H. J. A new method of preparing gold probes for multiple-labeling cytochemistry. *Eur. J. Cell Biol.* **38**, 87–93 (1985).
13. Sawaguchi, A. et al. Informative three-dimensional survey of cell/tissue architectures in thick paraffin sections by simple low-vacuum scanning electron microscopy. *Sci. Rep.* **8**, 7479 (2018).
14. Yokota, S. Effect of particle size on labeling density for catalase in protein A-gold immunocytochemistry. *J. Histochem. Cytochem.* **36**, 107–109 (1988).
15. Graham, R. C. Jr & Karnovsky, M. J. The early stages of absorption of injected horseradish peroxidase in the proximal tubules of mouse kidney: ultrastructural cytochemistry by a new technique. *J. Histochem. Cytochem.* **14**, 291–302 (1966).
16. Nakane, P. K. & Pierce, G. B. Jr Enzyme-labeled antibodies: preparation and application for the localization of antigens. *J. Histochem. Cytochem.* **14**, 929–931 (1967).
17. Mundel, P., Gilbert, P. & Kriz, W. Podocytes in glomerulus of rat kidney express a characteristic 44 KD protein. *J. Histochem. Cytochem.* **39**, 1047–1056 (1991).
18. Danilatos, G. Mechanisms of detection and imaging in the ESEM. *J. Microsc.* **160**, 9–19 (1989).
19. Newman, G. R., Jasani, B. & Williams, E. D. Metal compound intensification of the electron-density of diaminobenzidine. *J. Histochem. Cytochem.* **31**, 1430–1434 (1983).
20. von Ruhland, C. J. & Jasani, B. The amplification of polymerized diaminobenzidine with physical developers: sensitizing effects of transition metal salts and sulphide. *J. Microsc.* **238**, 111–122 (2009).
21. LaMer, V. K. Nucleation in phase transitions. *Ind. Eng. Chem.* **44**, 1270–1277 (1952).
22. Hsu, S. M. & Soban, E. Color modification of diaminobenzidine (DAB) precipitation by metallic ions and its application for double immunohistochemistry. *J. Histochem. Cytochem.* **30**, 1079–1082 (1982).
23. Green, M. A., Sviland, L., Malcolm, A. J. & Pearson, A. D. Improved method for immunoperoxidase detection of membrane antigens in frozen sections. *J. Clin. Pathol.* **42**, 875–880 (1989).
24. Scopsi, L. & Larsson, L. I. Increased sensitivity in peroxidase immunocytochemistry. A comparative study of a number of peroxidase visualization methods employing a model system. *Histochemistry* **84**, 221–230 (1986).
25. Siegesmund, K. A., Yorde, D. E. & Dragen, R. A quantitative immunoperoxidase procedure employing energy dispersive X-ray analysis. *J. Histochem. Cytochem.* **27**, 1226–1230 (1979).
26. Nateghi, M. R., Mosslemin, M. H. & Hadjimohammadi, H. Electrochemical preparation and characterization of poly (3,3'-diaminobenzidine): a functionalized polymer. *React. Funct. Polym.* **64**, 103–109 (2005).
27. Leng, W., Pati, P. & Vikesland, P. J. Room temperature seed mediated growth of gold nanoparticles: mechanistic investigations and life cycle assessment. *Environ. Sci. Nano* **2**, 440–453 (2015).
28. Kumar, P. S. et al. High-yield synthesis and optical response of gold nanostars. *Nanotechnology* **19**, 015606 (2008).
29. Liebig, F. et al. A new route to gold nanoflowers. *Nanotechnology* **29**, 185603 (2018).
30. Privman, V. Mechanisms of diffusional nucleation of nanocrystals and their self-assembly into uniform colloids. *Ann. N. Y. Acad. Sci.* **1161**, 508–525 (2009).
31. Chen, X. & Wen, J. In situ wet-cell TEM observation of gold nanoparticle motion in an aqueous solution. *Nanoscale Res. Lett.* **7**, 598 (2012).
32. Tian, X., Zheng, H., Matsudaira, P. T. & Mirsaidov, U. Real time observation of gold nanoparticle aggregation dynamics on a 2D membrane. *Microsc. Microanal.* **22**, 808–809 (2016).
33. Li, C. et al. In-situ liquid-cell TEM study of radial flow-guided motion of octahedral Au nanoparticles and nanoparticle clusters. *Nano Res.* **11**, 4697–4707 (2018).
34. Woehl, T. J. et al. Direct observation of aggregative nanoparticle growth: kinetic modeling of the size distribution and growth rate. *Nano Lett.* **14**, 373–378 (2014).
35. Zheng, H., Mirsaidov, U. M., Wang, L. W. & Matsudaira, P. Electron beam manipulation of nanoparticles. *Nano Lett.* **12**, 5644–5648 (2012).
36. Zayats, M., Baron, R., Popov, I. & Willner, I. Biocatalytic growth of Au nanoparticles: from mechanistic aspects to biosensors design. *Nano Lett.* **5**, 21–25 (2005).
37. McGilvray, K. L. et al. Opportunistic use of tetrachloroaurate photolysis in the generation of reductive species for the production of gold nanostructures. *Phys. Chem. Chem. Phys.* **13**, 11914–11918 (2011).
38. Liu, X., Xu, H., Xia, H. & Wang, D. Rapid seeded growth of monodisperse, quasi-spherical, citrate-stabilized gold nanoparticles via H₂O₂ reduction. *Langmuir* **28**, 13720–13726 (2012).
39. Tangeysh, B. et al. Triangular gold nanoplate growth by oriented attachment of Au seeds generated by strong field laser reduction. *Nano Lett.* **15**, 3377–3382 (2015).
40. Ji, X. et al. Size control of gold nanocrystals in citrate reduction: the third role of citrate. *J. Am. Chem. Soc.* **129**, 13939–13948 (2007).
41. Sivaraman, S. K., Kumar, S. & Santhanam, V. Room-temperature synthesis of gold nanoparticles - size-control by slow addition. *Gold. Bull.* **43**, 275–286 (2010).
42. Kang, A. et al. pH-dependent size distribution of gold nanoparticles investigated by in situ pH-monitoring throughout the synthetic reaction. *Chem. Phys. Lett.* **639**, 230–233 (2015).
43. Liu, K. et al. A novel, rapid, seedless, in situ synthesis method of shape and size controllable gold nanoparticles using phosphates. *Sci. Rep.* **9**, 7421 (2019).
44. Sawaguchi, A., Aoyama, F., Ide, S. & Sugauma, T. The cryofixation of isolated rat gastric mucosa provides new insights into the functional transformation of gastric parietal cells: an in vitro experimental model study. *Arch. Histol. Cytol.* **68**, 151–160 (2005).
45. Sumi, T. et al. Disturbed blood flow induces erosive injury to smooth muscle cell-rich neointima and promotes thrombus formation in rabbit femoral arteries. *J. Thromb. Haemost.* **8**, 1394–1402 (2010).
46. Yoshii, A., Koji, T., Ohsawa, N. & Nakane, P. K. In situ localization of ribosomal RNAs is a reliable reference for hybridizable RNA in tissue sections. *J. Histochem. Cytochem.* **43**, 321–327 (1995).
47. Sawaguchi, A., Aoyama, F., Ide, S. & Sugauma, T. Capsule-supporting ring: a new device for resin embedding of glass-mounted specimens. *J. Microsc.* **234**, 113–117 (2009).

Acknowledgements

We thank E. Nakazawa and K. Ichikawa for scientific discussions and Y. Goto and Y. Todaka for technical assistance.

Author contributions

A.S. conceived the entire project, designed the protocol, performed low-vacuum SEM and TEM observations, wrote the manuscript, and drew all illustrations in Figs. 1, 5, and 9. T.K. performed elemental analysis by EDX-ray spectrometry. N.T., H.I., and F.A. performed sample preparation and immunocytochemistry for synaptopodin. A.Y. and Y.A. were involved in the pathological application. A.W. and T.S. performed HR-STEM analysis. N.C. and Y.H. applied in situ hybridization.

Competing interests

The authors declare no competing interests.

Additional information

Supplementary information The online version contains supplementary material available at <https://doi.org/10.1038/s42003-021-02246-3>.

Correspondence and requests for materials should be addressed to A.S.

Peer review information *Communications Biology* thanks the anonymous reviewers for their contribution to the peer review of this work. Primary Handling Editors: Dr Akhtar and Dr Karniski. Peer reviewer reports are available.

Reprints and permission information is available at <http://www.nature.com/reprints>

Publisher's note Springer Nature remains neutral with regard to jurisdictional claims in published maps and institutional affiliations.



Open Access This article is licensed under a Creative Commons Attribution 4.0 International License, which permits use, sharing, adaptation, distribution and reproduction in any medium or format, as long as you give appropriate credit to the original author(s) and the source, provide a link to the Creative Commons license, and indicate if changes were made. The images or other third party material in this article are included in the article's Creative Commons license, unless indicated otherwise in a credit line to the material. If material is not included in the article's Creative Commons license and your intended use is not permitted by statutory regulation or exceeds the permitted use, you will need to obtain permission directly from the copyright holder. To view a copy of this license, visit <http://creativecommons.org/licenses/by/4.0/>.

© The Author(s) 2021